Integrated Optical Components in Silicon for High Speed Analog-to-Digital Conversion

S. J. Spector, T. M. Lyszczarz, M. W. Geis, D. M. Lennon, J. U. Yoon,
M. E. Grein, R. T. Schulein
Lincoln Laboratory, Massachusetts Institute of Technology, 244 Wood St.,
Lexington, MA 02420, email: spector@ll.mit.edu

R. Amataya[a,b], J. Birge[a,b], J. Chen[a,b], H. Byun[a,b], F. Gan[a,b], C. W. Holzwarth[b,c], J. L. Hoyt[a,d], E. P. Ippen[a,b], F. X. Kärtner[a,b], A. Khilo[a,b], O. O. Olubuyide[a,d], J. S. Orcutt[a,b], M. Park[a,d], M. Perrott[a,d], M. A. Popović[a,b], T. Barwicz[a,b], M. Dahlem[a,b], R. J. Ram[a,b], and H. I. Smith[a,b]

[a]Department of Electrical Engineering and Computer Science, [b]Research Laboratory of Electronics,
[c]Department of Material Science and Engineering,
[d]Microsystems Technology Laboratories
Massachusetts Institute of Technology, 77 Massachusetts Avenue, Cambridge, MA 02139

ABSTRACT

Advances in femtosecond lasers and laser stabilization have led to the development of sources of ultrafast optical pulse trains that show jitter on the level of a few femtoseconds over tens of milliseconds and over seconds if referenced to atomic frequency standards. These low jitter sources can be used to perform opto-electronic analog to digital conversion that overcomes the bottleneck set by electronic jitter when using purely electronic sampling circuits and techniques. Electronic Photonic Integrated Circuits (EPICs) may enable in the near future to integrate such an opto-electronic analog-to-digital converters (ADCs) completely. This presentation will give an overview of integrated optical devices such as low jitter lasers, electro-optical modulators, Si-based filter banks, and high-speed Si-photodetectors that are compatible with standard CMOS processing and which are necessary for the implementation of EPIC-chips for advanced opto-electronic ADCs.

Keywords: Electronic photonic integrated circuits, silicon photonics, high index contrast, optical sampling, opto-electronic analog-to-digital conversion, femtosecond lasers

1. INTRODUCTION

Photonic analog-to-digital conversion techniques have been the subject of extensive research in recent years.[1-3] Photonic ADC architectures provide significant improvements over electronic ADC due to reduced clock jitter and the ability to channelize the sampled data for electronic quantization at lower data rates. Purely electronic sampling is currently limited by the inherent jitter of electronic circuits on the order of a quarter of a picosecond. Two standard architectures for photonic ADC systems have been discussed. The first, known as photonic time stretching, utilizes dispersion of a chirped optical pulse to temporally magnify a segment of a wideband signal to be sampled.[3] After magnification, the signal can be electronically sampled and quantized at a lower sample rate. Photonic time stretch systems suffer due to dispersion-induced attenuation of high-frequency components in the analog waveform. This distortion may be reduced using single sideband modulation,[4,5] but this approach complicates the system architecture. A

Silicon Photonics II, edited by Joel A. Kubby, Graham T. Reed, Proc. of SPIE Vol. 6477
64770O, (2007) · 0277-786X/07/$18 · doi: 10.1117/12.705219

second photonic ADC architecture is known as time-interleaved optical sampling. With this approach, a stream of pulses, or a single chirped pulse, is used to sample the analog signal at a high sample rate. After sampling, the pulses are separated into several lower-rate streams using time-division multiplexing (TDM)[6] or wavelength-division multiplexing (WDM)[7] techniques. The TDM approach simplifies the requirements on the optical sampling source. However, the TDM demultiplexer can be difficult to implement and may limit the maximum sample rate to a few GSa/s.

In this paper, we propose and analyze a new WDM approach, see Figure 1(a) and demonstrate the fabrication and utilization of some of the key components of this system. A low-jitter femtosecond laser with repetition rate $f_R = 1/T_R$ is emitting a stream of pulses that is spectrally broadened in highly nonlinear fiber (HNLF) and dispersed in single-mode fiber. Dispersion is chosen such that the chirped pulses cover the time interval between the pulses. The chirp may actually be chosen larger than necessary and the optical spectrum as then filtered by a bandpass filter to avoid aliasing of different optical frequency components in the following filter bank (see Figure (1b)) where filters with limited spectral range are used. The RF-waveform $V_{RF}(t)$ to be sampled is imprinted on the chirped pulse stream via a dual output silicon-based Mach-Zehnder electro-optic modulator (see Figure 1(b)). The differential optical output is channelized via a dual-WDM-filter bank with precisely-tuned center frequencies that map to certain sampling time slots. The signals from each channel correspond to time interleaved sample sequences that can be separately detected and both the difference and sum is digitized in low rate high resolution ADC's.

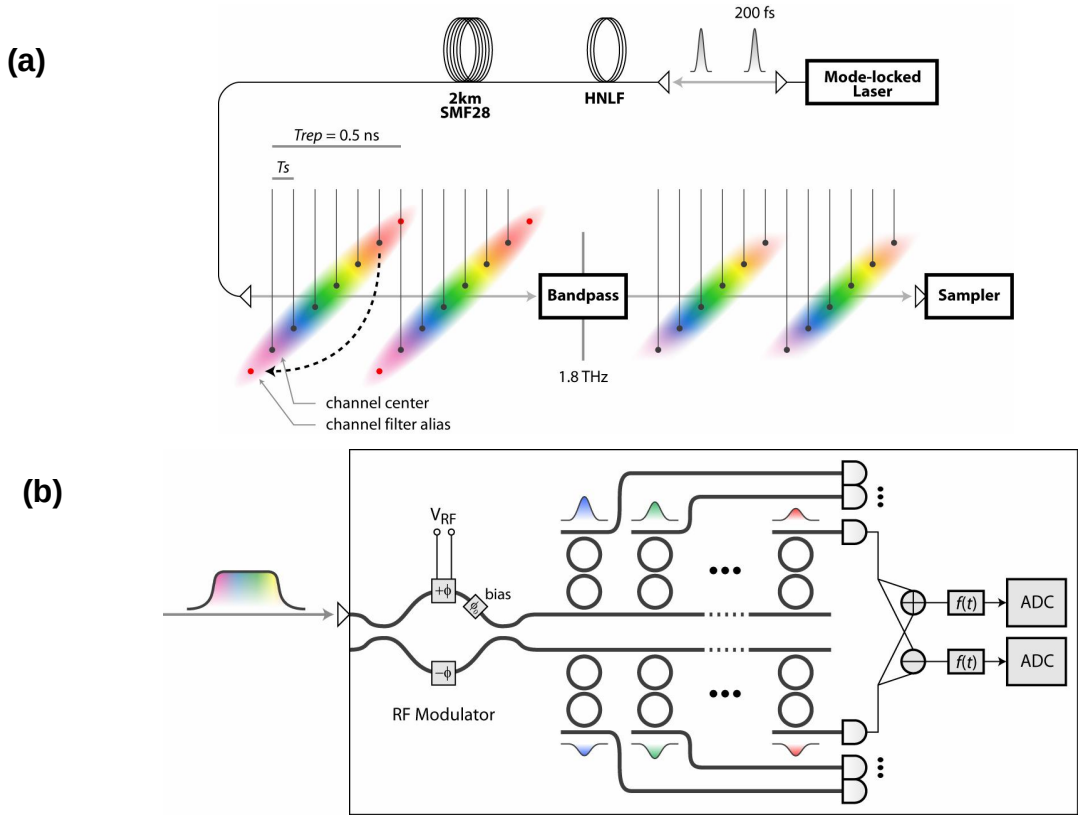

Figure 1: High-speed, high resolution optical sampling system and EPIC chip. (a) A low-jitter femtosecond laser with repetition rate $f_R = 1/T_R$ is emitting a stream of pulses that is spectrally broadened in highly nonlinear fiber (HNLF) and dispersed in regular single-mode fiber. Dispersion is chosen such that the chirped pulses cover the time interval between pulses with a smooth spectrum. The optical spectrum is limited by a bandpass filter. (b) The RF-waveform $V_{RF}(t)$ to be sampled is imprinted on the chirped pulse stream via a dual-port silicon-based electro-optic modulator. The differential optical output is channelized via a dual-WDM-filter bank with precisely-tuned center frequencies that map each optical frequency component to certain sampling time slots. The signals from each channel corresponding to time interleaved sample sequences are then separately digitized in low rate high resolution ADC's. The EPIC chip may comprise the silicon optical modulator, filter banks, detector arrays, the low rate electronic ADCs and feedback circuitry that is necessary to stabilize the optical filter bank.

Table 1 shows in the first column choices for system parameters such as laser repetition rate, filter bandwidth, channel spacing, number of filters, overall optical bandwidth to achieve an overall sampling rate of 40 or 100 GSa/sec. If a certain number of bits in resolution is to be supported when sampling a signal with an analog bandwidth at the Nyquist rate, i.e. half the sampling rate, the sampling jitter Δt and therefore the center frequency uncertainty Δf in the filter bank must be limited to

$$\Delta t = \frac{T_S}{\pi}\frac{\Delta V}{V} \qquad \Delta f = \frac{f_{Ch}}{T_S}\Delta t = \frac{f_{Ch}}{\pi}\frac{\Delta V}{V}. \tag{1}$$

The corresponding jitter and uncertainty in filter center frequencies for 40 or 100 GSa/sec can be found in the last two columns of Table 1.

Table 1: Summary of system parameters for overall sampling rates of 40 or 100 GSa/sec.

Overall Sampling Rate $f_S = 1/T_S$	Laser Rep. Rate $f_R = 1/T_R$	Filter Band-width Δf_{Ch}	Channel Spacing f_{Ch}	Number of Filters N	Total Optical Bandwidth Δf_{tot}	Resolution $\Delta V / V$	Max. Jitter Δt	Center Frequency Precision Δf
40 GSa/sec	2 GHz	25 GHz	80 GHz	20	1.6 THz	8 bit	30 fs	100 MHz
100 GSa/sec	2 GHz	25 GHz	80 GHz	50	4.0 THz	10 bit	3 fs	10 MHz

The low sampling jitter required, on the order of only a few femtoseconds, when approaching 1Tbit/sec sampling×resolution products is the reason for using optical techniques.

In the following analysis we consider a chirped pulse train $\bar{p}(t)$ given by

$$\bar{p}(t) = \sum_{k \in Z} p(t - kT_R). \tag{2}$$

Without loss of generality, we write the Fourier transform of an individual pulse as a baseband complex pulse times a quadratic dispersion term. Further we assume that individual pulses will not interfere with each other, which is enforced in Figure 1(a) by the bandpass filter. Thus, the analysis needs only be concerned with the action of the RF signal on an individual pulse, the spectrum of which is given by

$$P(\omega) = P_0(\omega)e^{iD_2(\omega)\omega^2/2}, \tag{3}$$

where $D_2(\omega)$ is the dispersion, that is assumed to change slowly versus frequency, such that it can be considered constant over the RF bandwidths involved; $P_0(\omega)$, the optical spectrum of the pulse, is allowed to be complex and may have higher order phase terms. The *usable* bandwidth of the pulse will be written as Δf_P. This bandwidth is defined as that portion which actually contributes to the final sampled signal. In this analysis, we assume that the spectrum is approximately constant over the usable bandwidth.

The electro-optic modulator is treated as a general multiplicative modulator, such that the modulated pulse in each ouput of the modulator can be written as

$$m(t) = s(t)\,p(t), \tag{4}$$

where the positive semi-definite signal $s(t)$ is the effective modulation. In general, $s(t)$ will not be the RF signal itself, but a related signal which takes into account the effect of the modulator model. This is the signal we seek to recover, and we assume that the modulator is such that its effects are invertible to obtain the actual RF signal. Finally, the modulated signal is analyzed by an n channel spectrometer with a spectral resolution of Δf_{ch}. There are some basic parameters bounds that can be determined from some simple feasibility considerations. The following conditions apply for a continuous sampler:

1. *Dispersion.* The individual pulses must be dispersed sufficiently such that they fill the repetition period T_R above a certain level.

2. *Temporal sampling.* To avoid cross talk between the samples, the impulse response of each channel filter must be shorter than T_R.

3. *Spectral sampling.* There must be sufficient spectral channels to adequately sample the modulated signal $s(t)$, which will have a bandwidth equal to or larger than that of $x(t)$.

The first item implies that the chirped pulse width should be larger than the repetition period. The second requirement—that the channel impulse response must be much shorter than the repetition rate—implies that the filter channel widths must be much larger than the repetition rate, or

$$\Delta f_{ch} >> f_R \tag{5}$$

This condition means that we need to have many comb lines in each channel. To avoid cross talk between the channels, the channel spacing f_{ch} must be larger than the channel width Δf_{ch}. Thus the total optical bandwidth is larger than the overall sampling rate $\Delta f_{tot} > f_s = nf_R$, which one would expect intuitively.

Next, we consider the action of the modulation on the optical spectrum. The final signal to be measured by the diodes will be related to the power spectrum $Q(\omega)$ of the optical spectrum before the filter banks

$$Q(\omega) \equiv |M(\omega)|^2 . \tag{6}$$

Here, $M(\omega)$ denotes the Fourier transform of the signal $m(t)$. The hope is that the time domain signal $s(t)$ can be uniquely extracted from this spectrum. Using the convolution theorem and straightforward analysis based on our assumptions detailed earlier (most notably the idea that the optical spectrum and its dispersion are constant over the RF bandwidth) the spectrum above is

$$Q(\omega) = \left| P_0(\omega) \int d\Omega\, e^{iD_2(\omega)\Omega^2/2} S(\Omega) e^{-iD_2(\omega)\omega\Omega} \right|^2 . \tag{7}$$

Thus this convolution integral is just an inverse Fourier transform with the change of variables $t \to D_2(\omega)\omega$. The "effective chirp" term $\exp[iD_2(\omega)\Omega^2/2]$ causes our modulation signal $s(t)$ to appear chirped with a dispersion identical to that of our optical signal. In most cases this will be a negligible effect, but if we treat the dispersion as constant it is a purely linear effect and can be trivially inverted. If we rewrite the chirped RF spectrum as $\tilde{S}(\omega) \equiv e^{iD_2\Omega^2/2} S(\Omega)$, we can express the final spectrum very simply in terms of its inverse transform:

$$Q(\omega) = \left| P_0(\omega) \tilde{s}[D_2(\omega)\omega] \right|^2 , \tag{8}$$

It is important to note that the above is an exact equation, and doesn't rely on any assumptions about the form of the optical pulse, other than it not contain spectral structure on the scale of the RF bandwidth. In other words, the unchirped optical pulse should look like an impulse response on the time scale of the RF signal, a reasonable criteria for a sampler. Also interesting is the prediction that the optical dispersion can potentially be "imprinted" on the RF signal we are measuring.

A significant outcome of this analysis is that the linearity of the dispersion and the smoothness of the optical spectrum are critical to the accurate functioning of the chirped pulse sampler. If these criteria are satisfied, such a sampler should be capable of measuring RF signals with bandwidths much higher than previously predicted, theoretically approaching the bandwidth of the optical pulse, if arbitrarily sharp filters can be used.

Using the two outputs of the modulator and generating the difference and sum of the dropped signals for each channel allows the following operations:

1.) The quasi static nonlinearities of the modulator can be removed from the signal.

2.) The intensity noise of the laser can be suppressed.

3.) The spectral shape of the modelocked laser pulses does not matter as long as it is smooth on a wavelength scale equal to the bandwidth of the RF-signal.

2. LOW JITTER FEMTOSECOND LASERS

The motivation for the optical analog-to-digital conversion comes from the fact that femtosecond optical pulse trains from low noise modelocked lasers even without using additional stabilization techniques easily show jitter levels in the few femtosecond range. Figure 2 (a) shows the schematic of a compact 200 MHz femtosecond fiber laser based on polarization additive pulse modelocking P-APM [8]. The laser operates in the soliton regime, i.e. with negative dispersion gain fiber and standard single mode fiber and generates 167 fs pulses with a FWHM spectral bandwidth of 2.5 THz (see Figure 2(b)). The timing jitter spectral density and integral timing jitter of this source is shown in Figure 2(c). For measurement times of less than 100 microseconds, i.e. for frequencies greater than 10 kHz, the integrated timing jitter is less than a few femtoseconds. The excessive low frequency timing jitter is of technical origin such as pump laser diode noise and can be further reduced if necessary. Nevertheless this source is already low jitter enough to enable the 40GSa/sec sampling experiment with parameters listed in the first row of Table 1. The necessary repetition rate of 2GHz can be achieved externally using repetition rate multiplication by locking for example to a high finess cavity. Parallel efforts are underway to integrate a similar femtosecond laser in chip scale format by using a SiGe-saturable Bragg reflector as the mode locking element and Er-waveguides as the gain medium [9].

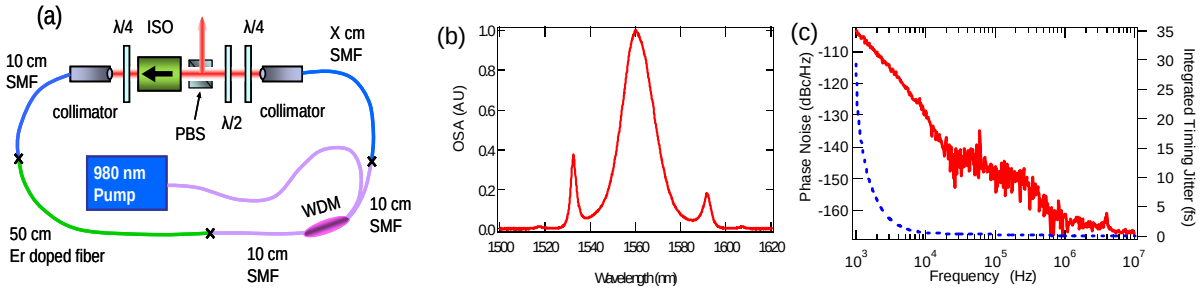

Figure 2: (a) Experiment Setup. (ISO: isolator; PBS: Polarization Beam Splitter) (b) Optical Spectrum, (c) Measured timing jitter spectral density (solid) and integrated timing (doted).

3. SILICON ELECTRO-OPTIC MODULATOR

Another important component of the sampling system is a high-speed silicon optical modulator that transfers the electronic signal into the optical domain. Very recently a modulator based on a MOS structure has been reported operating at up to 10GHz speed [10]. However, this device needs an applied voltage of 5 to 10V and $V_\pi L > 1$ V-cm which are both too large for CMOS applications. In this paper we describe a diode-based modulator that operates at low power and demonstrates 25% modulation depth at 10 GHz.

Fig. 3(a) illustrates the Mach-Zehnder interferometer device architecture used in these experiments. The interferometer arms contain diode sections, see Fig. 3(b), whose index can be changed by electronic carrier injection and the resulting plasma effect [11]. The output light intensity is modulated by the phase shifts induced in each arm of the interferometer by carrier injection. For the final implementation a dual output modulator that can be biased for equal output will be developed.

The modulators were fabricated with a standard CMOS-compatible lithography process. The fabricated waveguide dimensions are w×h=520nm×220nm. Aluminum is used as an electrical contact on top of the highly doped contact regions to minimize the contact resistance. The waveguide sidewalls are lightly doped to reduce resistance without incurring excessive optical loss [12-13]. Diodes were fabricated with p^+in^+ and p^+n doping. In forward biased operation of the p^+in^+ diode, the device speed is limited by carrier recombination. The p^+n diode can be used in reverse bias by modulating the width of the depletion region thereby sweeping carriers in and out of the waveguide. This configuration should achieve superior bandwidth at the expense of reduced sensitivity.

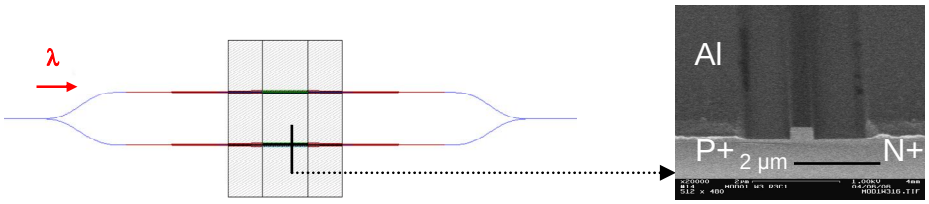

(a) (b)

Figure 3. Mach-Zehnder modulator. (a) Interferometer shown in plan view. (b) Cross section of diode structure. The silicon rib in the center of the micrograph functions as the optical waveguide and the diode. Current flow through the diode is laterally from the aluminum contacts on the left and right side of the photo. A thin silicon layer connects the metal contacts to the diode. This arrangement isolates the optical mode from the metal contacts and minimizes the optical loss.

The electrical to optical frequency response $|S_{21}|$ of a Mach-Zehnder modulator with 250-μm-long p^+in^+-sections in forward bias operation and a 6-mm-long p^+n device in reverse bias operation has been measured (see Figure 4.(a)). Under reverse bias the modulator is expected to have broad bandwidth because it is drift velocity dependent; $f_{3dB} = 2.4/2\pi\tau_{drift} \approx 80$ GHz [4] assuming the device reaches the drift velocity 10^7cm/s. However the measured f_{3dB} is just ~1 GHz. This indicates that the current experimental setup and device is RC delay limited. Due to fabrication problems, the metal contacts showed Schottky diode rather than ohmic characteristics. The induced large RC delay reduces the modulation bandwidth. Therefore the measured bandwidth is less than estimated. The response of the device under reverse bias is much weaker, thus it requires a longer arm length of 6.0 mm. The optimum bias voltage was ~-9 V with a current less than 2 μA for reverse bias operation.

Under forward bias, the electrical bandwidth f_{3dB} is about ~100 MHz. In this mode of operation the device bandwidth is carrier lifetime limited. The lifetime of this device is estimated to be τ = 1ns, $f_{3dB} \approx 1/2\pi\tau$ = 160 MHz, which is consistent with the measurement. The optimum bias voltage was ~1 V with a forward bias current of ~10 mA. The measured rf-power consumption for a 500-μm-long device for 25% modulation depth is shown in Fig. 4(b) together with the result obtained from analytical modeling. At low frequencies (10 MHz), only 1μW of RF drive power is necessary to achieve 25% modulation depth. At 10 GHz, 100 mW is needed. The relatively low electrical power dissipation ~100 mW at 10 GHz makes it possible to use a precompensation technique to increase the bandwidth of the 250-μm-long device. This is demonstrated by simulations. A simple high pass filter is connected in front of the p^+n diode modeled by a series resistor and diffusion capacitance and reactance as shown in the inset to Fig. 4(a), The high pass filter in the modulator driver circuit extends the bandwidth of the modulator from 100 MHz to 10 GHz as shown in Fig. 4(a) dashed line. In a practical implementation, an additional allpass filter needs to be added to compensate for the phase distortions of the high pass filter.

4. HIGH INDEX CONTRAST FILTER BANK

The next major component of on optical analog-to-digital converter is the dual filter bank. Microring-resonator filters utilizing high-index contrast (HIC) materials are ideal for large scale EPIC systems because of their ability to achieve the low loss and large free spectral range (FSR) needed while maintaining wavelength-scale dimensions. Design and Fabrication of HIC microring resonators has proved to be very challenging due to the decrease in critical feature size as well as increased sensitivity to roughness and dimensional errors [14-17]. The proposed ADC chip requires a large bank of microring-resonator filters with very accurately spaced resonant frequencies and low crosstalk between adjacent channels.

We have previously reported success in the fabrication of second-order microring-resonator filters using silicon-rich silicon nitride (n =2.2 @ 1550 nm) as the core material, silicon dioxide as the undercladding, and an air overcladding. The fabrication process for these filters, based on scanning-electron beam lithography and reactive-ion etching, was optimized to achieve high absolute dimensional accuracy and smooth vertical sidewalls as described in

[18]. Using the design shown in Figure 5a a filter response with 50 GHz bandwidth, 2.5 THz FSR, 1.5 dB drop loss, and less than 30 dB crosstalk was achieved. In order to fabricate a filter bank using this design it is necessary to be able to individually control the resonant frequency (i.e. optical path length) of each filter. This can be done during fabrication or by postfabrication tuning techniques, for best results a combination of both should be used.

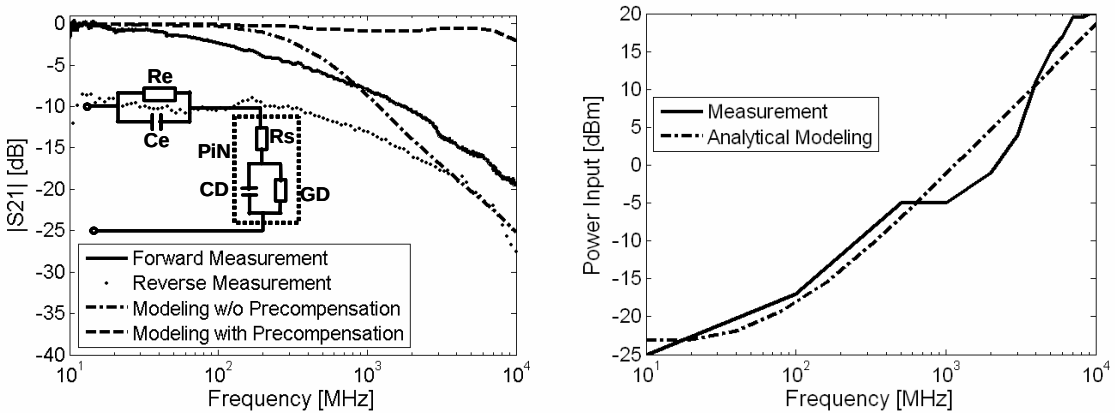

(a) (b)

Figure 4: (a) Frequency response of a 250-µm-long Mach-Zehnder interferometer: measurement under forward biasing (solid); MEDICI simulation without precompensation circuit (dash-dotted); MEDICI modeling with precompensation circuit (dashed; measurement of 6-mm-long reverse biased device (dotted). (b) Power consumption of a 500-µm-long Mach-Zehnder interferometer in forward bias with 25% modulation depth: Measurement (solid) and result from analytic model (dash-dotted).

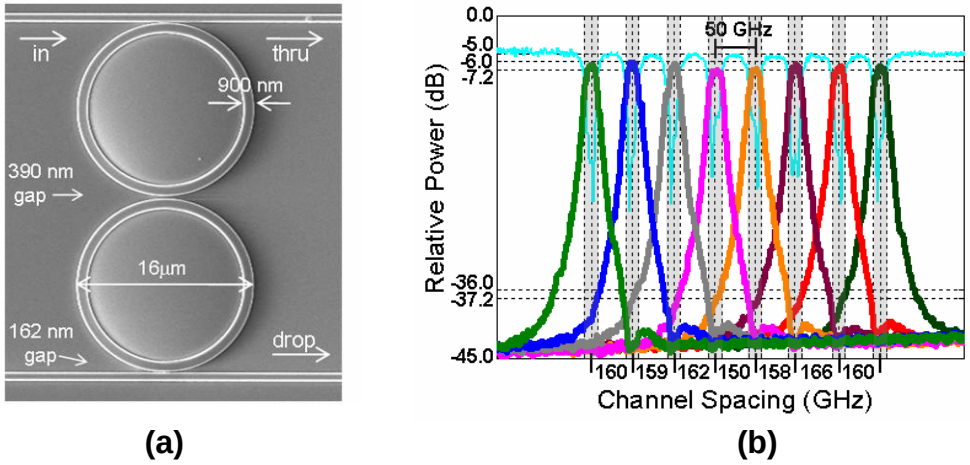

Figure 5: (a) Top view of second order microring resonator filter. (b) Filter response of eight-channel filter bank with a channel spacing of 150 GHz.

The first filter banks consisting of eight second-order filters were fabricated using the technique of dose modulation combined with small changes in ring radius to achieve accurate resonant frequency spacing. By using dose modulation, the technique of exposing each filter to a slightly different electron-beam dose, it is possible to change the average width of the rings with accuracy on the tens of picometers scale allowing for relative resonant frequency control

of a few GHz [19]. The fabricated filter banks with target channel spacings ranging from 90-180 GHz had actual channel spacings consistently 4-5% larger than expected and also a standard deviation in spacings of 4 GHz (Figure 5b). Through careful empirical calibration this 4-5% offset from the target can be reduced but the 5 GHz standard deviation in channel spacing, contributed to random process variations, cannot be corrected during fabrication. This means that to further increase the accuracy of the channel spacing a postfabrication tuning technique needs to be used. Of the many different methods of postfabrication tuning [20-22], thermal tuning with micro-heaters has the most benefits due to its ease of integration, dynamic tuning capabilities, and low power consumption.

Before micro-heaters for thermal tuning can be added to the current filter design an overcladding layer 1.5-2 μm thick needs to be added to optically insulate the modes propagating in the ring from the heater. This overcladding material needs to have a low refractive index, very low optical absorption, and be stable at high temperatures. It is also necessary that the overcladding material be able to fill the high-aspect-ratio gaps at the bus-to-ring coupling points. Silicon dioxide is the ideal candidate material for this layer but it is typically deposited by CVD, which tends to have trouble filling high-aspect-ratio gaps. As a cheaper and more reliable alternative we have started using hydrogen silsesquioxane (HSQ) as the overcladding material. HSQ, manufactured by DOW chemicals under the trade name FOx-25, is a spin-on dielectric with the chemical composition of $SiHO_{3/2}$. It is an attractive overcladding material for this application because of its excellent gap filling and planarization properties. However, after the normal thermal curing process the HSQ films have significant optical absorption due to Si-H bonds as well as a large tensile stress that limits the films maximum thickness to 1.2 μm [23].

We have investigated many different annealing processes in order to eliminate these problems and optimize the HSQ film for our application. We found that by rapid thermal annealing HSQ at temperatures above 1000ºC for 30s in an oxygen atmosphere it is possible to remove both the Si-H bonds and the tensile stress from the film. Through FTIR analysis it is evident that not only are the Si-H bonds removed but the film is fully converted into SiO_2 (Figure 6a). This is also supported by spectroscopic ellipsometer measurements that show that the refractive index of the film increased during annealing from 1.36 to 1.44 @ 1550 nm, the same as SiO_2. With the tensile stress of the film removed it is possible to use multiple coats to produce films over 2 μm thick (Figure 6b). We also confirmed that the superior gap filling properties of HSQ are maintained by filling high-aspect ratio gaps as large as 10:1 with this process. One last important test performed on the HSQ overcladding layer was to check that it would not increase the optical loss of the filters. For this test a weakly coupled ring resonator with a radius of 45 μm was fabricated out of stoichiometric silicon nitride (Si_3N_4). The quality (Q) factor of this ring was measured to be 240,000 which corresponds to a propagation loss in the ring of 1.5 dB/cm. This Q factor is similar to the highest reported measured Q values for Si_3N_4 ring resonators confirming that the annealed HSQ does not contribute significantly to the propagation loss [24].

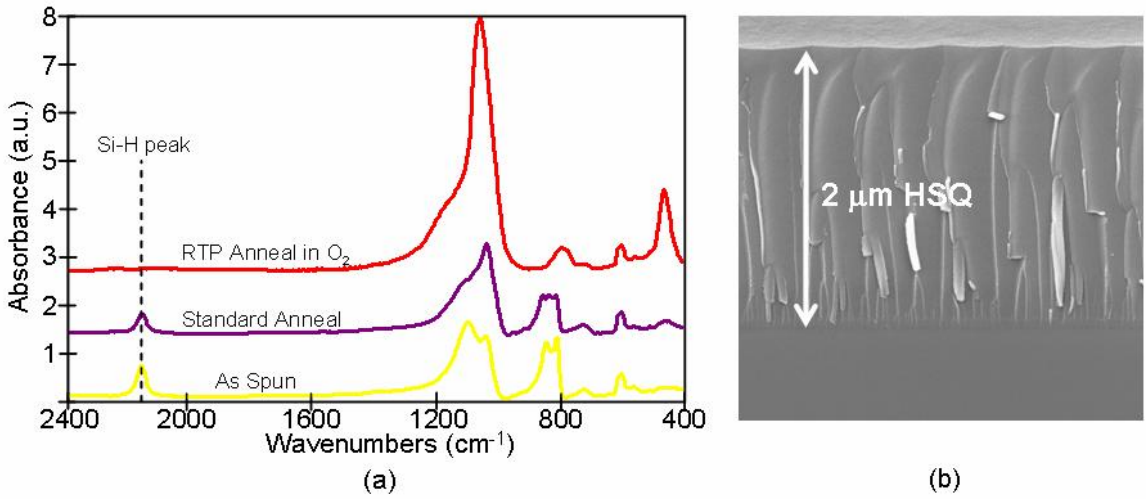

Figure 6: (a) FTIR spectra of HSQ as spun, after standard anneal, and after rapid thermal processing (RTP). (b) Cross-section view of 2 mm thick layer of HSQ fabricated using 4 spin coats.

As mentioned earlier, the thermal tuning with micro-heaters will be used for postfabrication tuning. The resonant wavelength is tuned via the temperature dependence of the refractive index of the waveguide. The thermo-optic coefficient ($\Delta n/\Delta T$) is temperature as well as wavelength dependent. At 1.55 mm, the thermo-optic coefficients for SiN and SiO_2 are 4×10^{-5} K^{-1} and 1.5×10^{-5} K^{-1} respectively. The theoretical tuning range for this waveguide is calculated to be 27 pm/K. Optimized thin film metal heaters (100 nm) are fabricated on top of the cladding to locally change the temperature of the resonator. One of the key parameters under consideration in the design of the heaters is the power dissipation per GHz of tuning. Finite-element thermal simulation (FEMLAB) gives the temperature profile for the filter with heaters on top showing approximately one dimensional heat flow with very low thermal cross-talk. The upper cladding of 1.5 μm ensures optical isolation of the resonator from local heaters on top. Simulations show long heaters with high thermal impedance are appropriate in order to minimize power dissipation for thermal tuning. The total tuning power for the finalized heater design is 60 μW/GHz with a tuning range of 150 GHz for 40 K change in the ring temperature.

To confirm the tuner designs before cladding deposition, we performed initial measurements on second-order filters with air as the upper cladding using external heaters. The change in center wavelength (Fig. 7) is approximately 36 pm/K. Due to slight variation in the group index of the waveguide with air cladding as compared to the HSQ cladding, the experimental tuning range is different from the theoretical value.

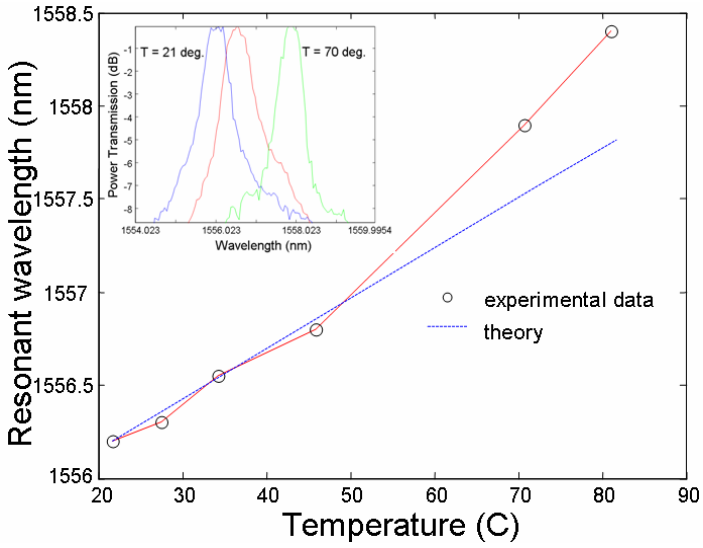

Figure 7: Thermal tuning for the second-order filter is observed by changing the temperature of the rings. A total shift of 2.2 nm is observed due to heating the rings from 21°C - 81°C. The inset shows the drop port spectra during tuning.

In addition to the filters fabricated in silicon nitride, there is an additional effort to fabricate ring resonator filter banks in silicon. These filters are fabricated using the same fabrication process and material as the silicon modulators, and therefore these components should be simple to integrate together. Because silicon has a higher index of refraction compared to silicon nitride, the fabrication of silicon filters is more challenging. Greater dimensional control is necessary to control the resonance of the filters, and any sidewall roughness will cause greater loss [25]. In addition, optical lithography is used in the process, which does not have the resolution of e-beam lithography or the ability to easily fine-tune the exposure of different features. However, optical lithography has much higher throughput, which will ultimately be necessary for manufacturing of these EPIC chips.

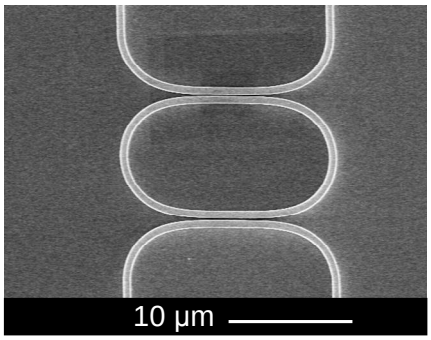

Figure 8: Racetrack resonator fabricated in SOI.

The coupling, between the input and output waveguides and the ring, together with the loss of the ring determine the overall loss of the device. A smaller gap than we can reliably fabricate (<170 nm) is necessary to achieve a 3 dB loss with our current process. One way to increase the coupling, without decreasing the gap size, is to lengthen the coupling region between the resonator and the waveguides. This is done by going to a racetrack instead of ring geometry. However, standard racetrack geometries introduce losses at the mode mismatch between the straight sections and the bends. A modified racetrack structure, as shown in Fig. 8, avoids this additional loss by smoothly increasing the radius of curvature from infinity (i.e., straight) to 5 µm over a short distance. The devices fabricated using this design have not shown any decrease in Q when compared to similar ring resonators. The additional coupling length (approximately 4 µm) increases the required gap size by about 50 nm which simplifies the lithography. The significant downside to this method is a decrease in free spectral range by 32% when compared to a ring resonator with a radius of curvature of 5 µm.

The racetrack resonator shown in Fig. 8 has waveguides 500 nm wide, 210 nm thick, and has a gap of 200 nm. The Q-factor for this device is 8000, and the loss of the drop channel is 3 dB when compared to a straight waveguide of similar length. Devices with larger gaps have Q-factors around 20,000, but the loss increases to 5-7 dB. Multichannel filters, with 5 channels, were also fabricated. Fig. 9 shows the resonant frequencies of the 5 channels. The designed spacing was 43 GHz (0.34 nm). The maximum channel-to-channel error is 87 GHz (0.68 nm). All the channels had Q factors near 8000, and losses between 1-3 dB, except for channel 4. Because the resonance frequencies of channel 2 and 4 overlap, the channel 2 resonator dropped all the light at that frequency leaving little light for channel 4. Future devices will add thermal tuning to correct for these errors in resonant frequency. Errors of 100 GHz can be corrected with temperature changes of 15 °C, which should be straight forward to achieve [26,27].

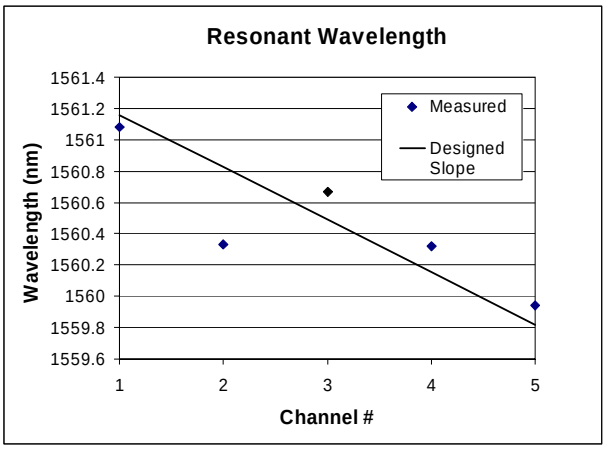

Figure 9: Measured resonance frequencies of the multichannel filter compared to the designed channel spacing.

5. SILICON INFRARED PHOTODIODES

Previously, we have investigated Ge-photodiodes for detecting the optical output of the filterbank [9]. Here, we investigate another approach to fabricating high speed photo detectors on the silicon platform. All-Si, CMOS-compatible, waveguide photodiodes were fabricated with a 10 to 20 GHz bandwidth, responsivity from 1270 to 1740 nm (0.8 A W^{-1} at 1550 nm), and leakage current of 0.37 µA [28]. As shown in Fig. 10, these p-i-n diodes are similar to the diode structure in the modulator. The diodes consist of an intrinsic Si waveguide 500×220 nm, where the optical mode is confined, and two thin, 50-nm-thick, doped Si wings that extend 5 µm out from either side of the waveguide. The Si wings, which are doped one p-type and the other n-type, make electrical contact to the waveguide with minimal effect on the optical mode. The edges of the wings are metallized to increase electrical conductivity. Ion implantation of Si^{+} $1x10^{13}$ cm^{-2} at 190 keV into the waveguide produces crystal damage, increasing the optical absorption from 2 to 3 dB cm^{-1} to 70 to 100 dB cm^{-1}, and causing the generation of a photo current when the waveguide is illuminated with sub-bandgap radiation. These diodes can be annealed to 450 °C during fabrication and still maintain their photoresponse and bandwidth. This thermal stability is believed to be due to an oxygen-stabilized divacancy complex formed during ion implantation [29].

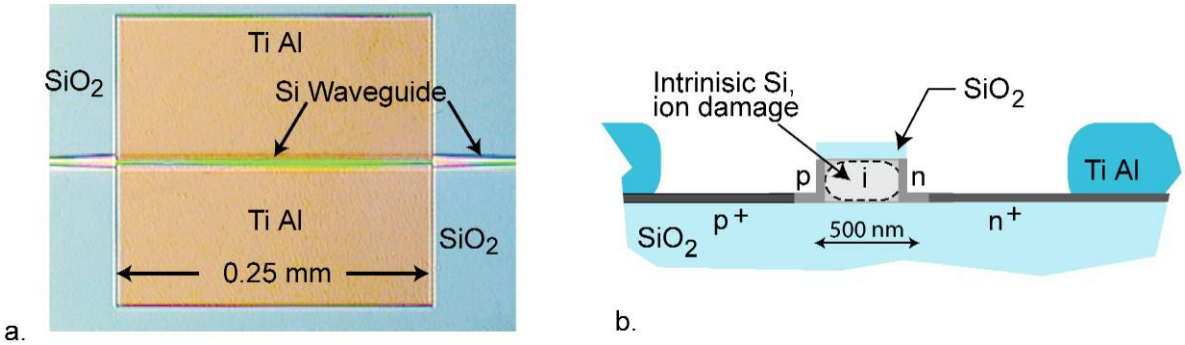

Figure 10. Waveguide photodiode. (a) Top-view optical micrograph of 0.25-mm-long waveguide photodiode. (b) Schematic drawing of the p-i-n diode cross section. The waveguide is the intrinsic silicon rib in the center of the sketch.

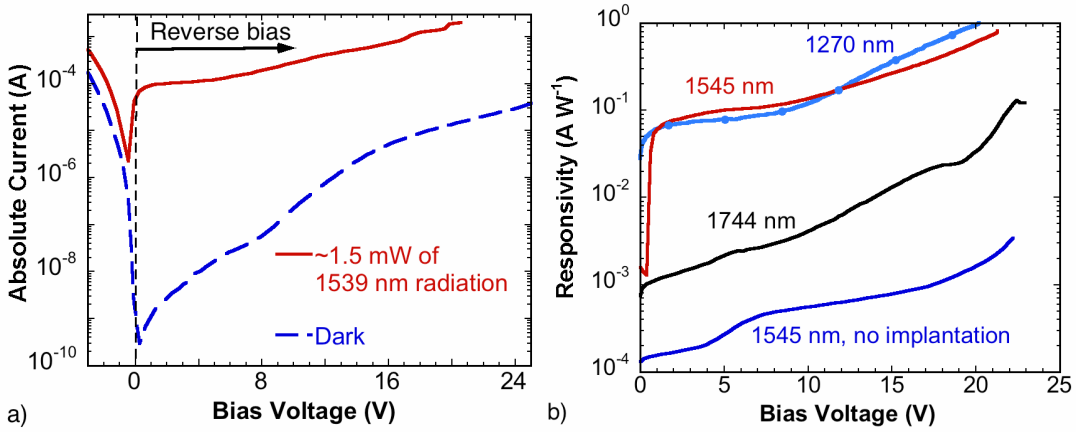

Figure 11: Photodiode optical properties. (a) Current-voltage characteristics for a photodiode in the dark and illuminated. (b) Responsivity, which is the ratio of photodiode current to the light entering the diode, for an implanted diode at 1270, 1545 and 1744 nm and an unimplanted diode at 1545 nm.

The current-voltage curves of the silicon-implanted diode, shown in Fig. 10, illuminated with 1545-nm radiation and in the dark are shown in Fig. 11(a). With an optical absorption of ~ 100 dB cm $^{-1}$ only 50% of the incoming light is absorbed in the 0.25mm long diode, the rest passing out the other end. At large bias voltages, >15 V, the responsivity exceeds unity quantum efficiency, indicating carrier multiplication is occurring. These photodiodes exhibit linear photoresponse with light intensity and operate over a broad range of wavelengths as shown in Fig. 11(b). Unimplanted diodes also exhibit a linear photoresponse, but the low light absorption results in a photoresponsivity of < 0.003 A W^{-1}.

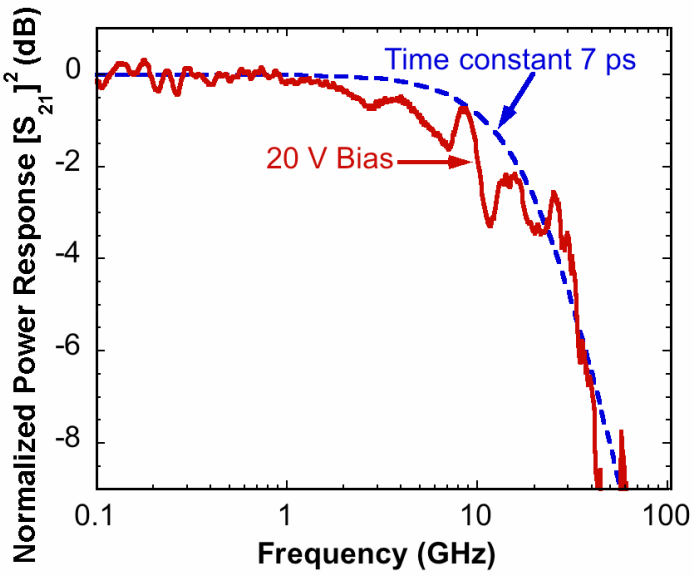

Figure 12: Photodiode frequency response. The response for an RC time constant of 7 ps is shown for comparison.

The photodiodes' frequency responses were measured using a vector network analyzer and an optical modulator capable of 50-GHz operation. Figure 12 shows the photodiode frequency response after correcting for the frequency response of the modulator. The half-power point is between 10 and 20 GHz, which is consistent with the 7-ps time constant calculated from the contact pad capacitance of 0.14 pF and the 50-Ω load.

Earlier work done on similar diodes, as first described by Knights et al. [30], had a smaller responsivity, limiting these diodes to monitoring optical power. The transition from a power-monitoring device to a robust high-frequency photodiode is the result of reducing the waveguide dimensions from ~5 to ~0.5 µm and optimizing the implantation in the Si waveguide. The smaller waveguide results in a larger overlap between the optical mode and the damaged region, thereby increasing optical absorption, reducing the required device length, and increasing the frequency response.

6. CONCLUSIONS

In this paper, we discussed an improved opto-electronic ADC-scheme, that mitigates modulator nonlinearities and laser noise, and is integrable on an electronic-photonic silicon platform. Such systems are bound to overcome the sampling limitations set by pure electronic systems due to jitter. Some of the key components of the system such as low jitter femtosecond modelocked lasers, filter banks, modulators, and detectors have been discussed. Progress in the design and fabrication of these devices has been presented.

ACKNOWLEDGEMENTS

The Lincoln Laboratory portion of this work was sponsored by the EPIC Program of the Defense Advanced Research Projects Agency and in part by the Department of the Air Force under Air Force Contract FA8721-05-C-0002. The MIT portion of this work was sponsored by the DARPA EPIC Program under contract W911NF-04-1-0431. Opinions, interpretations, conclusions, and recommendations are those of the authors, and do not necessarily represent the view of the United States Government.

REFERENCES

[1] P.W. Juodawlkis, J. C. Twichell, G. E. Betts, J. J. Hargreaves, R. D. Younger, J. L. Wasserman, F. J. O'Donnell, K. G. Ray, and R. C. Williamson, "Optically sampled analog-to-digital converters," IEEE Trans. Microwave Theory Tech. **49**(10), 1840 (2001).

[2] T. R. Clark, J. U. Kang, and R. D. Esman, "Performance of a time- and wavelength-interleaved photonic sampler for analog-digital conversion," IEEE Photon. Technol. Lett. **11**(9), 1168 (1999).

[3] F. Coppinger, A. S. Bhushan, and B. Jalali, "Photonic time stretch and its application to analog-to-digital conversion," IEEE. Trans. Microwave Theory Tech. 47(7), 1309 (1999).

[4] J. M. Fuster, D. Novak, A. Nirmalathas, and J. Marti, "Single-sideband modulation in photonic time-stretch analogue-to-digital conversion," Electron. Lett. 37, 67 (2001).

[5] Y. Han, B. Jalali, J. Han, B. Seo, H. Fetterman, "Demonstration and analysis of single sideband photonic time-stretch system," IEICE Trans. Electron. E86-C(7), 1276 (2003).

[6] J. A. Bell, M. C. Hamilton, D. A. Leep, H. F. Taylor, and Y. –H. Lee, "Optical sampling and demultiplexing applied to A/D conversion," Devices for Optical Processing, 1562, 276 (1991).

[7] M. Y. Frankel, J. U. Kang, and R. D. Esman, "High-performance photonic analogue-to-digital converter," Electron. Lett. 33(25), 2096 (1997).

[8] J. Chen, J. W. Sickler, E. P. Ippen, and F. X. Kärtner, "High repetition rate, low jitter, fundamentally mode-locked soliton Er-fiber laser," submitted to Conference on Lasers and Electro-Optics CLEO, Baltimore, US, 2007.

[9] F. X. Kärtner, S. Akiyama, G. Barbastathis, T. Barwicz, H. Byun, D. T. Danielson, F. Gan, F. Grawert, C. W. Holzwarth, J. L. Hoyt, E. P. Ippen, M. Kim, L. C. Kimerling, J. Liu, J. Michel, O. O. Olubuyide, J. S. Orcutt, M. Park, M. Perrott, M. A. Popović, P. T. Rakich, R. J. Ram, H. I. Smith, and M. R. Watts, "Electronic Photonic Integrated Circuits for High Speed, High Resolution Analog to Digital Conversion," SPIE Conference Photonic West, San Jose, January 2006.

[10] A. Liu, Dean Samara-Rubio, L. Liao, and M. Paniccia. "Scaling the Modulation Bandwidth and Phase Efficiency of a Silicon Optical Modulator". IEEE J. of Selected Topics in Quantum Electronics, Vol. 11, No. 2, March/April 2005.

[11] R.A. Soref, "Silicon-based optoelectronics," Proc. IEEE 81, 1687–1706 (1993).

[12] F. Gan and F. X. Kärtner, "High-speed Silicon Electro-optic Modulator Design," IEEE Photonics Technology Letters, 17, 1007-1009, (2005).

[13] F. Gan, F. J. Grawert, J. Schley, S. Akiyama, J. Michel, K. Wada, L. C. Kimerling, F. X. Kärtner, "Design of All-Optical Switches Based on Carrier-Injection in Si/SiO2 Split-Ridge Waveguides (SRW's)", IEEE J. of Lightwave Technology 2006, Vol.24, No. 9, September 2006.

[14] B.E. Little, S.T. Chu, H.A. Haus, J. Foresi, and J.-P. Laine, "Microring resonator channel dropping filters," Journal of Lightwave Technology 15, 998 (1997).

[15] B.E. Little, J.S. Foresi, G. Steinmeyer, E.R. Thoen, S.T. Chu, H.A. Haus, E.P. Ippen, L.C. Kimerling, and W. Greene, "Ultra-compact Si-SiO2 microring resonator optical channel dropping filters," IEEE Photonics Tech. Lett., 10, 549 (1998).

[16] H. A. Haus, "Microwaves and Photonics," in OSA TOPS 23 Symposium on Electro-Optics: Present and Future, H. A. Haus, Ed., pp. 2-8, Optical Society of America, Washington, DC (1998).

[17] B.E. Little, “Advances in microring resonators,” in Proc. Integrated Photonics Research Conf., pp. 165-167 (2003).

[18] T. Barwicz, M.A. Popović, M.R. Watts, P.T. Rakich, E.P. Ippen and H.I. Smith, “Fabrication of Add-Drop Filters Based on Frequency-Matched Microring Resonators”, Journal of Lightwave Technology 24, 2207 (2006).

[19] C.W. Holzwarth, T. Barwicz, M. A. Popović, P. T. Rakich, F. X. Kaertner, E. P. Ippen, and H. I. Smith, “Accurate resonant frequency spacing of microring filters without postfabrication trimming,” Journal of Vacuum Science and Technology B 24 3244 (2006).

[20] D.K. Sparacin, C. Hong, L.C. Kimerling J. Michel, J.P. Lock, and K.K. Gleason, “Trimming of microring resonators by phot-oxidation of a plasma-polymerized organosilane cladding material,” Optics Letters, 30 2251 (2005).

[21] G.N. Nielson, “Micro-opto-mechanical switching and tuning for integrated optical systems,” Ph.D. dissertation, MIT, Jul. 6, 2004.

[22] D.H. Geuzebroek, E.J. Klein, H. Kelderman, and A. Driessen, “Wavelength tuning and switching of a thermo-optic microring resonator,” Proc. ECIO 395 (2003).

[23] H.C. Liou and J. Pretzer, “Effect of curing temperature on the mechanical properties of hydrogen silsesquioxane thin film,” Thin Solid Films, 335 186 (1998).

[24] J. Guo, M.J. Shaw, G.A. Vawter, G.R. Hadley, P. Esherick, and C.T. Sullivan, “High-Q microring resonator for biochemical sensors,” Proc. SPIE 5728 83 (2005).

[25] K. K. Lee, D. R. Lim, H-C Luan, A. Agarwal, J Foresi, and L. C. Kimerling, “Effect of size and roughness on light transmission in a Si/SiO2 waveguide: Experiments and model,” App. Phys. Lett., 77, 1617-1619 (2000).

[26] R. L. Espinola, M.-C. Tsai, J. T. Yardley, and R. M. Osgood, “Fast and low-power thermooptic switch on thin silicon-on-insulator,” IEEE Photon. Technol. Lett., 15, 1366–1369 (2003).

[27] M. W. Geis, S. J. Spector, R. C. Williamson, and T. M Lyszczarz, “Submicrosecond submilliwatt silicon-on-insulator thermooptic switch,” App. Phys. Lett., 77, 1617-1619 (2004).

[28] M. W. Geis, S. J. Spector, M. E. Grein, R. T. Schulein, J. U. Yoon, D. M. Lennon, S. Deneault, F. Gan, F. X. Kaertner, and T. M. Lyszczarz, “CMOS-compatible, all-Si, high-speed, waveguide photodiodes with high responsivity in near-infrared communication bands,” to be published in IEEE Photon. Technol. Lett.

[29] A. P. Dolgolenko, P. G. Litovchenko, M. D. Varentsov, G. P. Gaidar, and A. P. Litovchenko, “Particularities of the formation of radiation defects in silicon with low and high concentration oxygen,” Phys. Status Solidi B 243, no. 8, pp. 1842-1852 (2006).

[30] J. K. Doylend, P. J. Foster, J. D. G. Bradley, P. E. Jessop, and A. P. Knights, “Integrated Silicon Waveguide-based Structures for Terminal Detection of 1550 nm,“ 2006 3rd IEEE International Conference on Group IV Photonics Sept. 2006 Ottawa On Canada, IEEE Proceedings cat. #06EX1276C, pp.161-163.